NUCLEAR SCIENCE AND ENGINEERING: **135**, 103–122 (2000)

Differential Sampling Applied to Mammography Image Simulation

Douglas E. Peplow*

Oak Ridge National Laboratory
Building 6025 Mailstop 6363, P.O. Box 2008
Oak Ridge, Tennessee 37831-6363

and

Kuruvilla Verghese

North Carolina State University
Department of Nuclear Engineering
Raleigh, North Carolina 27695

Received June 1, 1999
Accepted November 23, 1999

Abstract—*Differential sampling is a powerful tool that allows Monte Carlo to compute derivatives of responses with respect to certain problem parameters. This capability has been implemented within an in-house Monte Carlo code that simulates detailed mammographic images from two new digital systems. Differential sampling allows for the calculation of the first and all second derivatives of all of the different tallies computed by the code as well as the first and second derivatives of the mammographic image itself with respect to material parameters, such as density and cross sections. The theory behind differential sampling is explained, the methodology for implementation into the imaging code is discussed, and two problems are used to demonstrate the power of differential sampling.*

I. INTRODUCTION

Mammography is the X-ray radiographic technique that is designed for breast imaging. The lifetime risk of developing breast cancer is one out of nine for women in the United States, and the earlier the tumor is detected, the better is the prognosis for survival. X-ray mammography has enabled early detection of tumors and has led to a large increase in survivability. At present, annual mammograms are indicated for all women more than 50 yr (postmenopausal) and for high-risk women in younger age groups. Contrast in the images is greater in the higher age groups because of the higher adipose tissue content of their breasts, as compared to premenopausal women who have more glandular tissue than adipose. Although advances in mammography have resulted in image contrast enhancement, the goal of mammography is to improve the detection of smaller tumors in premenopausal women without increasing the radiation dose. Methods that do not use radiation, such as ultrasound and magnetic resonance imaging, are at present not competitive with X-ray mammography for routine cancer screening.

Mammogram images are formed just like standard X-ray images. A beam of X rays is passed through the tissue and then strikes a film. Areas of higher density will absorb more X rays (transmitting less), resulting in a lower exposure to the film. If X rays were only either transmitted or absorbed, the image captured by the film would perfectly show which areas of the tissue absorbed more photons. Unfortunately, X rays can also scatter in the tissue. Scattered X rays can strike the film in any location, adding a constant level of exposure to the entire image.

*E-mail: peplowde@ornl.gov

Standard clinical mammography systems use an X-ray tube bremsstrahlung spectrum that is filtered to remove very low energy photons. A conical X-ray beam is transmitted through the breast that is compressed between two flat plastic paddles. The transmitted beam passes through an antiscatter grid to a phosphor screen, and the image is recorded on photographic film. The grid removes some of the scattered X rays but increases the amount of source photons needed and increases the absorbed dose in the breast. The tube anode potential is adjusted to suit the breast thickness.

Image contrast is degraded by scattered radiation striking the detector and geometric blurring by nonpoint sources and diverging beams, and by detection systems themselves. The high-energy portion of a tube anode spectrum does not add much information to the image because of low-interaction cross sections. The low-energy portion of the spectrum only increases dose to the breast since low-energy photons have a very high interaction cross section and are rarely transmitted. Only the mid-range of photon energies contributes to the contrast seen in the images. The optimum photon energy range for compressed breast thicknesses of 3 to 6 cm is ~17 to 25 keV.

There have been both evolutionary and revolutionary responses to the need to enhance mammography to the point of detecting smaller tumor masses earlier. Improvements in film quality, scatter rejection grids, better digital detectors, and better computer image enhancements are all leading to clearer mammograms in this country. Many manufacturers of current mammography machines are developing new systems that have digital data acquisition and scanning slots to further decrease the amount of scattered radiation—all with the goal of an improved image. These systems still use the tube anode and a bremsstrahlung spectrum of X rays but are improvements over the conventional film/screen systems.

Research groups in this country and abroad are working on completely new mammography technologies using intense monoenergetic beams of X-ray radiation from synchrotron sources.[1–3] Images produced from the monoenergetic, parallel, polarized synchrotron radiation show better contrast than conventional images, approaching the theoretical limit for an X-ray attenuation image. With the tunable monoenergetic beam, a clear optimization can be made for contrast and dose. The parallel aspect of synchrotron radiation allows for large air gaps between the patient and detector, greatly reducing the effect of scatter without any magnification or geometric blurring.

This work stems from a collaboration with the group that started research in synchrotron mammography.[4] The goal of the project is to develop a set of modeling tools that could be used to compare the performance of the new synchrotron system to the next generation of scanning-slot mammography systems that are being tested in clinics and hospitals. Sensitivities to various material parameters and perturbation calculations are of interest to this group and others in medical physics. The longer range goal is to use these modeling tools to optimize new mammography systems.

The best way to quantify the effects of scattered radiation in the images from different systems and also compare other system effects is to create a Monte Carlo tool capable of simulating the complete image. Digital mammograms are typically 2048 × 2048 pixels in size as a minimum. Tallying photons into more than four million pixels poses some challenges to any Monte Carlo code because of the potentially high variance in each of the pixels. A combination of variance-reduction methods made it possible to simulate accurate images using real pixel dimensions within reasonable computation times. The complete method of image simulation, including the application of noise and the modulation transfer function (MTF), both of which tend to smear images, has been presented by the authors elsewhere.[5] Simulated images of two common mammography phantoms on both the digital Fischer Senoscan scanning-slot system and the synchrotron-based mammography system showed excellent agreement with actual digital images taken on the two systems.

This paper will focus on differential sampling and how it was applied to the image simulation problem. Using differential sampling, Monte Carlo can calculate not only the desired response but also the derivative of that response to some parameter. These derivatives can be used to determine sensitivities of dose-to-material parameters or sensitivity of image contrast to tumor density. They can also be used to propagate uncertainties in the material data to find the final dose uncertainty. With a truncated Taylor series, the derivatives can be used in perturbation studies. A demonstration of how differential sampling can be used to provide more (and useful) information for imaging problems appears in Sec. V.

II. THE MCMIS MONTE CARLO IMAGING CODE

The Monte Carlo Mammography Image Simulation[5] (MCMIS) is a detailed code specifically for the simulation of digital mammography systems, including scanning-slot systems. This code was written so that three variance-reduction techniques can be used together to create images with realistic pixel sizes. These are source rastering, the separation of the scattered and unscattered image, and the point-detector scheme.[6] The source rastering is just a form of stratified sampling and ensures that the images do not suffer from mottle caused by random source sampling. The point-detector method forces a score to every pixel in the image at each photon interaction, thus decreasing the variance of the final scattered image. Since the scattered image does not show the detail that the unscattered images show, it can be calculated on a coarse mesh, saving computation time.

In the energy range of medical imaging, the coherent scattering distribution from amorphous materials, such as tissues and plastics, differs a great deal from the scattering distributions predicted by the free-gas model.[7] One example is shown in Fig. 1. Both of the mammography systems studied here are well collimated, which eliminates photon scatter through more than a few degrees from the image. In the small-angle range, the difference between the measured and predicted coherent scatter distributions is very large, and the amount of incoherent scatter is small. To make the simulation of mammography systems as complete as possible, we measured the molecular coherent scattering form factors of mammography related materials.[8] These measurements used a unique two-step approach that accurately accounted for incoherent scatter and multiple scatter. The measurements were performed using monoenergetic synchrotron radiation, which makes the final form factors for these materials the most accurate and detailed that are currently available.

MCMIS uses four problem description input decks and various cross-section tables, and it outputs several image files and their associated stochastic uncertainties. The code contains four source models, three detector geometries, and three digital detector types. These models and all of their parameters are listed in one of the input decks. The geometry of the object being imaged and a list of materials are listed in other input decks. The last input deck contains information for the Monte Carlo run, i.e., the number of histories, variance-reduction methods to use, etc. In addition to the image, this code also calculates for each geometry region four tallies: the energy deposited, the total flux, the exposure, and the dose.

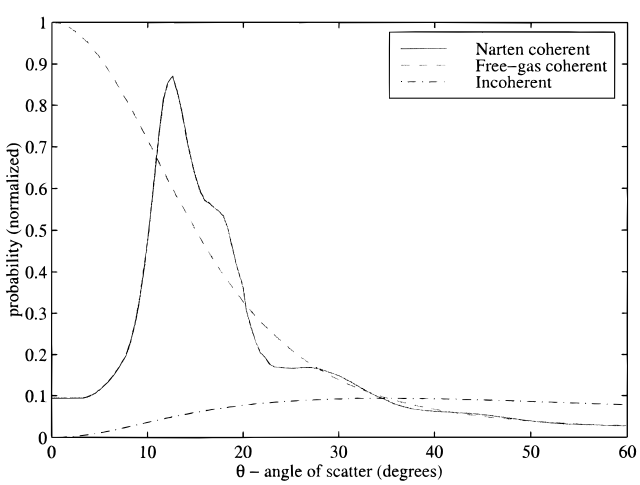

Fig. 1. Coherent scattering distributions in water for 18-keV photons using atomic form factors (dashed line) and using Narten's[7] measured molecular form factor (full line). The incoherent scattering (dash-dot line) is also displayed.

The models include both a parallel synchrotron source and a divergent point source for the Senoscan. The synchrotron system uses a Fuji imaging plate ($BaFBr_{0.85}I_{0.15}$) detector, and the Senoscan uses a CsI charge-coupled-device detector. The photon interaction types are coherent scatter, incoherent scatter, and the photoelectric effect. Cross sections include elements up to calcium and are tabulated for energies between 1 and 300 keV, appropriate for medical imaging. Implicit capture and the last-flight estimator variance-reduction techniques are available as options. The code does model polarization effects in the scattering interactions, which is required to simulate the synchrotron-based mammography system. Extensive comparisons with other calculations of scattering, dose, and scanning-slot responses were made[5] to verify the accuracy of MCMIS.

A series of steps are taken to simulate the actual image. First, the fine-mesh unscattered image and the coarse-mesh scattered image are added together. Then, noise, in an amount corresponding to actual noise seen in real images, is added to the image, and the MTF is applied. The MTF of the synchrotron system accounts for the smearing that occurs when the image plate is read by the laser scanner and converted into a digital image. The MTF of the Senoscan accounts for the blur caused by the focal spot size and blur introduced by the detector system. For polyenergetic sources, multiple monoenergetic runs of the code are made and then added together using the source spectrum as the weighting function. A comparison of images of the American College of Radiography (ACR) phantom created by MCMIS and taken on the real synchrotron imaging system is shown in Fig. 2. The image taken with the synchrotron shows vertical streaks caused by slight deformities in the crystal used to select the single energy of the beam. Measured contrast for items in real digital images and the Monte Carlo simulations matched very well. A more complete description of the methods, testing, and verification of both images and dose calculations made by MCMIS have been presented in an earlier paper.[5]

III. DIFFERENTIAL SAMPLING

Monte Carlo has the ability to calculate derivatives of responses with respect to certain input parameters at the same time it calculates the response itself. This is called differential sampling, and some uses of such derivatives include

1. *Perturbation studies*: Instead of running the Monte Carlo code multiple times, a base response r can be calculated as a function of the set of input parameters $\mathbf{p}$. If this code also calculates the derivatives of the response

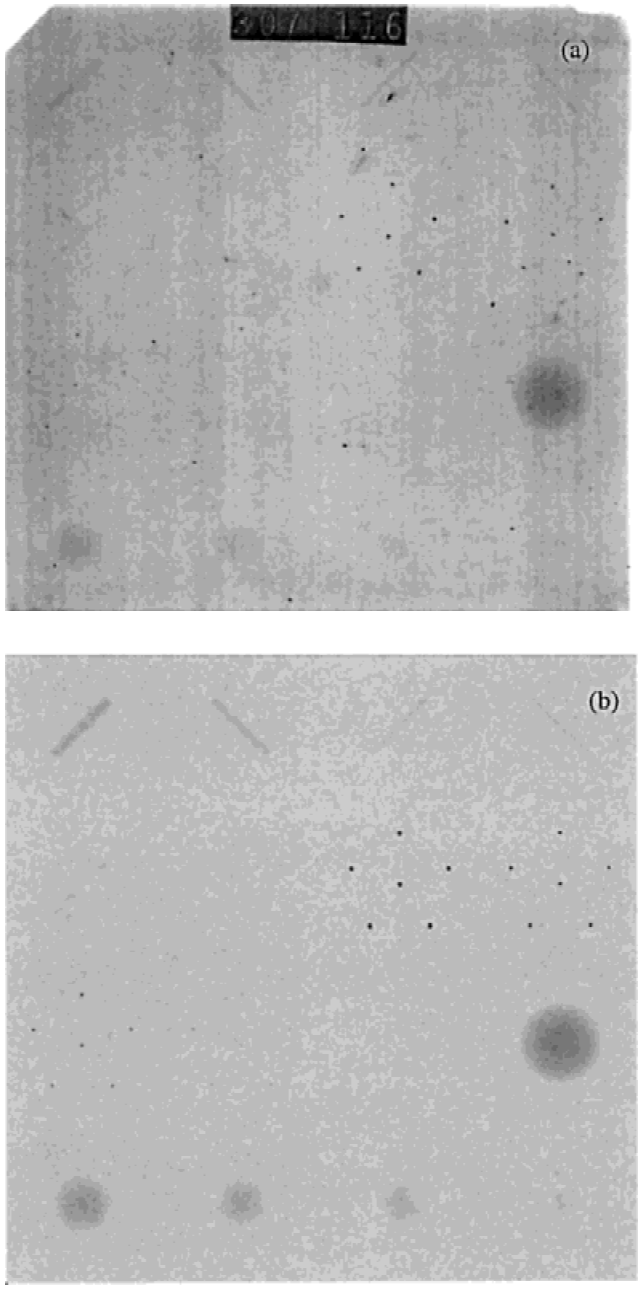

Fig. 2. Images of the ACR phantom: (a) image measured with the synchrotron system at 18 keV with a 5-mm slot size and (b) MCMIS Monte Carlo simulation.

with respect to each parameter $\partial r/\partial p_i$, and the second derivatives $\partial^2 r/\partial p_i \partial p_j$, and so on, then the value of the response for a small perturbation of $\mathbf{p}$ can be found for any set of parameters by a Taylor series expansion. Thus,

$$r(\mathbf{p} + \boldsymbol{\delta}\mathbf{p}) = r(\mathbf{p}) + \sum_i \left(\frac{\partial r}{\partial p_i} \right) \delta p_i + \frac{1}{2} \sum_i \sum_j \left(\frac{\partial^2 r}{\partial p_i \partial p_j} \right) \delta p_i \delta p_j + \cdots \quad . \tag{1}$$

In practice, the series has to be truncated after a few terms (usually after the second-order terms), and therefore, it is only applicable for values of $(\mathbf{p} + \boldsymbol{\delta}\mathbf{p})$ close to $\mathbf{p}$. Correlated sampling calculates all of the perturbed cases along with the reference case; differential sampling calculates the perturbed cases outside of the Monte Carlo code. If a new perturbation case is to be investigated, no more code runs would be required once the reference case and its derivatives had been found.

2. *Sensitivity studies*: The derivatives $\partial r/\partial p_i$ can also be used to find the sensitivity of the response to uncertainties in the input parameters. For example, which cross sections affect the response the most and need to be known with the highest accuracy? Differential sampling can reveal this.

3. *Total error*: The uncertainty expressed in most Monte Carlo studies is only the stochastic uncertainty from the calculation. This does not represent the propagated uncertainties from any of the input parameters. With the sensitivities found by differential sampling, the total uncertainty can be stated for a Monte Carlo response.

Differential sampling can be applied to many problems, even reactor problems, and can also be used in conjunction with variance-reduction techniques.

This section will describe the system used to calculate the derivatives of Monte Carlo–calculated responses and how they were implemented in the image simulation code. The descriptions in this paper start with the Monte Carlo games as they are practiced, as opposed to starting with the Boltzmann transport equation as in the pioneering papers by Rief.[9–12] The approach presented here is written with the Monte Carlo practitioner in mind.

III.A. Monte Carlo Game Description

The response calculated by a Monte Carlo game is simply the average of the individual responses resulting from the many histories. For a game where multiple contributions to the response tally are made during a history, the final average $\bar{r}$ has the form

$$\bar{r} = \frac{1}{N} \sum_{i=1}^{N} \sum_{j=1}^{J} c_{ij} \prod_{k=1}^{j} P_{ik} \quad , \tag{2}$$

where each segment j of history $i = 1$ to N makes some contribution c_{ij} to the response tally, weighted by the product of segment probability densities $\prod_{k=1}^{j} P_{ik}$ up to

that point in the history. The notation used here is similar to that used by Perel, Wagschal, and Yeivin.[13] As pointed out by of Rief,[9] these probability densities are either transport T or collision C probabilities. Thus,

$$\prod_{k=1}^{j} P_{ik} = T_{i1} C_{i1} T_{i2} C_{i2} \cdots \quad , \tag{3}$$

ending in either an absorption or escape in the J'th segment. Of course, the quantities P_{ik} are not explicitly calculated and multiplied together to form the product but are instead the result of the various stochastic choices made during the history of J segments.

An example of a game like this would be the calculation of flux by the path-length estimator. Each time the particle crosses a region, the path length (the contribution c_{ij}) multiplied by the product of the segment probabilities up to this point $\prod_{k=1}^{j} P_{ik}$ is added to a subtally. The product is equal to w, the current weight[a] of the particle (or 1 if no variance-reduction methods have been employed). As the history continues, if the particle again crosses the same region, the new path length multiplied by the current weight is added to the subtally. At the end of the history, the subtally value is added to the main response tally, and the square of the subtally is added to the variance tally.

The foregoing game description can also be used for games where splitting or point detectors are being used. When a particle is at a given point in the history, the contribution to a point detector or other tally is made, and then the history continues on. The methods to calculate derivatives for these biased Monte Carlo games are the same as for the basic games.

III.B. First Derivatives

The derivative of the final Monte Carlo response with respect to a problem parameter a is

$$\frac{\partial}{\partial a} \bar{r} = \frac{\partial}{\partial a} \left[\frac{1}{N} \sum_{i=1}^{N} \sum_{j=1}^{J} c_{ij} \prod_{k=1}^{j} P_{ik} \right] \tag{4}$$

$$= \frac{1}{N} \sum_{i=1}^{N} \sum_{j=1}^{J} \left(c_{ij} \prod_{k=1}^{j} P_{ik} \right) \times \left\{ \frac{1}{c_{ij}} \frac{\partial}{\partial a} c_{ij} + \sum_{k=1}^{j} \frac{1}{P_{ik}} \frac{\partial}{\partial a} P_{ik} \right\} \quad . \tag{5}$$

This form contains the score made to the response subtally $c_{ij} \prod_{k=1}^{j} P_{ik}$, multiplied by a term containing the relative derivative of the contribution and the sum of the relative derivatives of the segment probability densities. With each path segment, the response for the segment $r_{ij} = c_{ij} \prod_{k=1}^{j} P_{ik}$ (computed as $r_{ij} = wc_{ij}$, where w is the weight) is added to the response subtally. At the same time, the subtally q_a^i for the derivative is also updated with

$$q_a^i = \sum_{j=1}^{J} (r_{ij}) \left\{ \frac{1}{c_{ij}} \frac{\partial}{\partial a} c_{ij} + t_a^{ij} \right\} \quad , \tag{6}$$

where t_a^{ij} is the current value of the relative segment probability derivative accumulator, up to this segment,

$$t_a^{ij} = \sum_{k=1}^{j} \frac{1}{P_{ik}} \frac{\partial}{\partial a} P_{ik} \quad . \tag{7}$$

The real key is then finding the expressions for relative derivatives $(1/P_{ik})(\partial/\partial a)P_{ik}$ for both the collision and transport kernels for every parameter a and the relative derivative of the contributions $(1/c_{ij})(\partial/\partial a)c_{ij}$.

At the end of the history, when the response subtally is added to the main response tally and its square is added to its associated variance tally, each derivative subtally is added to the main derivative tally, and its square is added to a variance tally for the derivative. Let

$$A_a = \sum q_a^i \tag{8}$$

and

$$B_a = \sum (q_a^i)^2 \quad . \tag{9}$$

At the end of the Monte Carlo calculation, A_a is used for finding the derivative (the sensitivity) with respect to parameter a, and B_a is used for finding the standard deviation of the derivative:

$$\frac{\partial}{\partial a} \bar{r} = \frac{1}{N} A_a \tag{10}$$

and

$$\sigma_{\partial \bar{r}/\partial a} = \sqrt{\frac{1}{N} \left[\frac{1}{N} B_a - \left(\frac{\partial}{\partial a} \bar{r} \right)^2 \right]} \quad . \tag{11}$$

III.C. Double Derivatives

Derivatives with respect to any combination of two parameters (including second derivatives) of the Monte Carlo response $\bar{r}$ can also be calculated. The double partial derivative of the response for the game described earlier with respect to the parameters a and b is

[a] The photon weight is the probability of the photon being at this point in the simulation had the simulation been an analog one. It is the ratio of the true probability distribution to the biased probability distribution (each evaluated at the value of the sampled quantity).

$$\frac{\partial}{\partial b}\frac{\partial}{\partial a}\bar{r} = \frac{\partial}{\partial b}\frac{\partial}{\partial a}\left[\frac{1}{N}\sum_{i=1}^{N}\sum_{j=1}^{J} c_{ij}\prod_{k=1}^{j} P_{ik}\right] \tag{12}$$

$$= \frac{1}{N}\sum_{i=1}^{N}\sum_{j=1}^{J}\left[\left(c_{ij}\prod_{k=1}^{j} P_{ik}\right)\left\{\sum_{k=1}^{j}\frac{1}{P_{ik}}\frac{\partial^2}{\partial a\partial b}P_{ik} - \sum_{k=1}^{j}\left(\frac{1}{P_{ik}}\frac{\partial P_{ik}}{\partial a}\right)\left(\frac{1}{P_{ik}}\frac{\partial P_{ik}}{\partial b}\right)\right.\right.$$
$$+\left(\sum_{k=1}^{j}\frac{1}{P_{ik}}\frac{\partial}{\partial a}P_{ik}\right)\left(\sum_{k=1}^{j}\frac{1}{P_{ik}}\frac{\partial}{\partial b}P_{ik}\right) + \frac{1}{c_{ij}}\frac{\partial^2}{\partial a\partial b}c_{ij}$$
$$\left.\left.+\left(\frac{1}{c_{ij}}\frac{\partial}{\partial a}c_{ij}\right)\left(\sum_{k=1}^{j}\frac{1}{P_{ik}}\frac{\partial}{\partial b}P_{ik}\right) + \left(\frac{1}{c_{ij}}\frac{\partial}{\partial b}c_{ij}\right)\left(\sum_{k=1}^{j}\frac{1}{P_{ik}}\frac{\partial}{\partial a}P_{ik}\right)\right\}\right] . \tag{13}$$

This can be more conveniently expressed as

$$\frac{\partial}{\partial b}\frac{\partial}{\partial a}\bar{r} = \frac{1}{N}\sum_{i=1}^{N}\sum_{j=1}^{J}\left[(r_{ij})\left\{t^{ij}_{1,a,b} - t^{ij}_{2,a,b} + t^{ij}_a t^{ij}_b + \frac{1}{c_{ij}}\frac{\partial^2}{\partial a\partial b}c_{ij} + t^{ij}_a\frac{1}{c_{ij}}\frac{\partial}{\partial b}c_{ij} + t^{ij}_b\frac{1}{c_{ij}}\frac{\partial}{\partial a}c_{ij}\right\}\right] , \tag{14}$$

where the two new accumulators (types 1 and 2) are

$$t^{ij}_{1,a,b} = \sum_{k=1}^{j}\frac{1}{P_{ik}}\frac{\partial^2}{\partial a\partial b}P_{ik} , \tag{15}$$

$$t^{ij}_{2,a,b} = \sum_{k=1}^{j}\left(\frac{1}{P_{ik}}\frac{\partial P_{ik}}{\partial a}\right)\left(\frac{1}{P_{ik}}\frac{\partial P_{ik}}{\partial b}\right) , \tag{16}$$

and t^{ij}_a and t^{ij}_b are already being kept for the calculation of the first derivative. During the history, every time the response subtally is updated, the subtally for each double partial derivative is updated:

$$q^i_{a,b} = \sum_{j=1}^{J}\left[(r_{ij})\left\{t^{ij}_{1,a,b} - t^{ij}_{2,a,b} + t^{ij}_a t^{ij}_b + \frac{1}{c_{ij}}\frac{\partial^2}{\partial a\partial b}c_{ij}\right.\right.$$
$$\left.\left.+ t^{ij}_a\frac{1}{c_{ij}}\frac{\partial}{\partial b}c_{ij} + t^{ij}_b\frac{1}{c_{ij}}\frac{\partial}{\partial a}c_{ij}\right\}\right] \tag{17}$$

using the current values of the $t^{ij}_{1,a,b}$, $t^{ij}_{2,a,b}$, t^{ij}_a, and t^{ij}_b accumulators.

At the end of the history, when the response subtally is added to the main response tally, each double partial derivative subtally is added to the main double partial derivative tally, and its square is added to the derivative variance tally:

$$A_{a,b} = \sum q^i_{a,b} \tag{18}$$

and

$$B_{a,b} = \sum (q^i_{a,b})^2 . \tag{19}$$

Then, at the end of the game, $A_{a,b}$ is used for finding the double derivative, and $B_{a,b}$ is used for calculating the variance of the double derivative.

The relative derivatives of the contributions and of the transport/collision kernels have not been discussed yet since they are problem dependent. The easiest way to understand these is through an example. Most problems will have similar T and C kernels and the contributions depend on what responses (tallies) one is trying to determine.

More details on the foregoing differential sampling methods and more examples of implementation into simple problems are available elsewhere.[14]

IV. APPLICATION TO THE IMAGING CODE

MCMIS-DS, an extension of MCMIS for differential sampling, provides the same four tallies (responses) for each geometry region, namely, the energy deposited E_d, the total flux ϕ, the exposure X, and the dose D. Of course, exposure is reported only when the region happens to consist of air. The parameters that one might be interested in investigating include the density ρ of a region and its partial or total cross sections $\mu = \mu^{phot} + \mu^{coh} + \mu^{inc}$.

Because cross sections are actually energy-dependent, trying to find the derivative of a response, such as energy deposited in a region, with respect to a particular cross section could only be done at exactly one specific energy. Another way to look at this problem is this: Suppose one did calculate the derivative of response r with respect to cross section p. In calculating a truncated Taylor series to do a perturbation study,

$$r(p+\delta p) = r(p) + \left(\frac{\partial r}{\partial p}\right)\delta p + \frac{1}{2}\left(\frac{\partial^2 r}{\partial p^2}\right)(\delta p)^2 + \cdots , \tag{20}$$

one would find that describing δp would be difficult since it is a function of energy and the response r is only a scalar.

The way MCMIS-DS overcomes this problem is by defining the total macroscopic cross section of a region as the weighted sum of the three interaction cross sections

for photoelectric effect, coherent scatter, and incoherent scatter. That is,

$$\mu(E) = a^{phot}\mu^{phot}(E) + a^{coh}\mu^{coh}(E) + a^{inc}\mu^{inc}(E) \ , \tag{21}$$

where the constants a^i are all equal to 1 for an unperturbed case. The code then finds the derivative of the responses with respect to one of the a^i constants. This way, the energy dependence problem is avoided, and perturbations can be cast in a form of one partial cross section's increasing (a^{phot} going from 1 to 1.1) and another partial cross section's decreasing (a^{coh} going from 1 to 0.9). This system is also somewhat easier for the user compared to finding derivatives with respect to relative cross sections (μ^i/μ) as others do,[9] since there is no ambiguity about how the other cross sections are changing when a study of one of the interaction cross sections is changing. With the foregoing system, it is obvious that the total cross section does change. So, MCMIS-DS has four parameters for derivatives: the density and the three reaction-type multipliers—a^{phot}, a^{coh}, and a^{inc}—for each region.

MCNP (Ref. 15) has the ability to calculate perturbations on the weight fraction of a certain element in a compound. Since MCMIS-DS evaluates cross sections by region at the beginning, this type of perturbation could not be included. Also, the code uses measured molecular form factors for coherent scatter, so the effect of a weight fraction change for a given element in a molecular material could not be found since the form factor could be measured only at the nominal weight fraction values. One should also be careful here since increasing one weight fraction implies that the others are also decreasing. It is not clear from the MCNP manual how this is taken into consideration.

For a problem of R regions, four tallies in each region (the energy deposited, the total flux, the exposure, and the dose), and four parameters in each region to vary, there are $4R$ responses, $16R^2$ first derivatives, and $8R^2(4R+1)$ double derivatives. For a small problem of ten regions, this works out to more than thirty thousand values, with thirty thousand associated uncertainties. This amount of information would be too much for any user, so MCMIS-DS does not keep track of every derivative.

MCMIS-DS allows the user to select one region where the four tallies are the only four responses investigated. Derivatives and double derivatives are found with respect to the four variables in one or two regions (four or eight total parameters). This way, only the derivatives of interest are calculated and stored by the program, which saves time and disk space. These regions are listed in a separate input file that is read by the program with the other input decks for geometry, cross section, etc.

The unscattered image is a matrix of tallies that could number in the millions, depending on the number of pixels. The coarse-mesh unscattered image can also be viewed as a large matrix of tallies. Again, for time and storage reasons, only a single first derivative and a single second derivative of the image are found with respect to only one of four parameters of one region. The derivatives of the unscattered images are calculated with the analytic calculation of the unscattered image. The derivatives of the scattered images are calculated by the Monte Carlo differential-sampling methods described in the this paper.

IV.A. Derivatives of the Kernels

The Monte Carlo game consists of two kernels: transport T and collision C. These are expressed as probability densities and are sampled by the Monte Carlo game.

The transport kernel is expressed as

$$T = \rho_M \mu_M \exp\left(-\sum \rho_m \mu_m s_m\right) \tag{22}$$

for a particle that crosses many regions m with a path length of s_m in each and finally interacts in region M. Using the notation from Sec. IV for the energy-dependent mass attenuation coefficients, the total mass attenuation coefficient in each region is

$$\mu_m = a_m^{phot}\mu_m^{phot} + a_m^{coh}\mu_m^{coh} + a_m^{inc}\mu_m^{inc} \ , \tag{23}$$

where the values of the a_m^i's are 1.

The relative derivative of the transport kernel is then found to be

$$\frac{1}{T}\frac{\partial T}{\partial \rho_m} = \begin{cases} -\mu_m s_m & m \neq M \\ -\mu_m s_m + 1/\rho_m & m = M \ , \end{cases} \tag{24}$$

with respect to any of the region densities. With respect to one of the cross-section coefficients a_m^i, where the interaction type i is photoelectric, coherent, or incoherent, the relative derivative of the transport kernel is

$$\frac{1}{T}\frac{\partial T}{\partial a_m^i} = \begin{cases} -\rho_m \mu_m^i s_m & m \neq M \\ -\rho_m \mu_m^i s_m + \mu_m^i/\mu_m & m = M \ . \end{cases} \tag{25}$$

The collision kernels for interaction type i is (in the material where the reaction is taking place)

$$C_{phot} = \frac{a^{phot}\mu^{phot}}{\mu} \tag{26}$$

$$C_{coh} = \frac{a^{coh}\mu^{coh}}{\mu} P^{coh}(\mathbf{\Omega} \rightarrow \mathbf{\Omega}') \tag{27}$$

$$C_{inc} = \frac{a^{inc}\mu^{inc}}{\mu} P^{inc}(\mathbf{\Omega}, E \rightarrow \mathbf{\Omega}', E') \ , \tag{28}$$

where the P^i terms represent the scattering distributions for photons of direction and energy of $\mathbf{\Omega}, E$ to scatter to direction and energy of $\mathbf{\Omega}', E'$. The relative derivative of the collision kernel for reaction type k with respect to the cross-section multiplier a^i is (suppressing the subscript m)

$$\frac{1}{C_k}\frac{\partial C_k}{\partial a^i} = \begin{cases} -\mu^i/\mu & i \neq k \\ -\mu^i/\mu + 1/a^i & i = k \ . \end{cases} \tag{29}$$

Since none of the collision kernels depend on the density of the material, $(1/C_k)(\partial C_k/\partial\rho) = 0$. Derivatives of the collision kernels in one region with respect to a parameter in another region are also 0.

The double partial derivatives of the transport kernel can also be found to be

$$\frac{1}{T}\frac{\partial}{\partial\rho_m}\frac{\partial}{\partial\rho_n}T = \begin{cases} \mu_m s_m \mu_n s_n & m \neq M,\ n \neq M \\ \mu_m s_m \mu_n s_n - \dfrac{\mu_n s_n}{\rho_m} & m = M,\ n \neq M \\ \mu_m s_m \mu_m s_m - 2\dfrac{\mu_m s_m}{\rho_m} & m = n = M\ , \end{cases} \tag{30}$$

$$\frac{1}{T}\frac{\partial}{\partial a_m^i}\frac{\partial}{\partial a_n^j}T = \begin{cases} \rho_m \mu_m^i s_m \rho_n \mu_n^j s_n & m \neq M,\ n \neq M \\ \rho_m \mu_m^i s_m \rho_n \mu_n^j s_n - \dfrac{\mu_m^i}{\mu_m}\rho_n \mu_n^j s_n & m = M,\ n \neq M \\ \rho_m \mu_m^i s_m \rho_m \mu_m^j s_m - 2\dfrac{\mu_m^i}{\mu_m}\rho_m \mu_m^j s_m & m = n = M\ , \end{cases} \tag{31}$$

and

$$\frac{1}{T}\frac{\partial}{\partial a_m^i}\frac{\partial}{\partial\rho_n}T = \begin{cases} \rho_m s_m \mu_n s_n \mu_m^i & m \neq M,\ n \neq M,\ m \neq n \\ \rho_m s_m \mu_n s_n \mu_m^i - s_m \mu_m^i & m \neq M,\ n \neq M,\ m = n \\ \rho_m s_m \mu_n s_n \mu_m^i - \dfrac{\mu_n s_n}{\mu_m}\mu_m^i & m = M,\ n \neq M \\ \rho_m s_m \mu_n s_n \mu_m^i - \dfrac{\rho_m s_m}{\rho_n}\mu_m^i & m \neq M,\ n = M \\ \rho_m s_m \mu_m s_m \mu_m^i - 3 s_m \mu_m^i + \dfrac{\mu_m^i}{\rho_m \mu_m} & m = n = M\ , \end{cases} \tag{32}$$

and the double partial derivatives of the collision kernels are (again, suppressing the subscript m)

$$\frac{1}{C_k}\frac{\partial}{\partial a^i}\frac{\partial}{\partial a^j}C_k = \begin{cases} 2\dfrac{\mu^i}{\mu}\dfrac{\mu^j}{\mu} & i \neq k,\ j \neq k \\ 2\dfrac{\mu^i}{\mu}\dfrac{\mu^j}{\mu} - \dfrac{\mu^j}{a^i\mu} & i = k,\ j \neq k \\ 2\dfrac{\mu^i}{\mu}\dfrac{\mu^j}{\mu} - 2\dfrac{\mu^i}{a^i\mu} & i = j = k\ . \end{cases} \tag{33}$$

Any double derivative of any of the collision kernels with respect to density is zero.

IV.B. Derivatives of the Tally Contributions

The relative derivatives of the tally contributions must also be found with respect to each of the parameters. Each of the four responses and the point-detector contribution for the scattered image calculation will be considered in turn.

IV.B.1. Energy Deposited

The first response is the energy deposited in a region. In an analog game, the contribution is just $c = E$, the current energy of the particle for a photoelectric effect or $c = E_e$, the energy of the Compton electron for an incoherent scatter. The relative derivatives of these with respect to the density of a region or any of the cross-section coefficients are zero. If implicit capture is being used, the contribution at each interaction is then $c = Ea^{phot}\mu^{phot}/\mu$. The relative derivatives are then similar to that of the photoelectric collision kernel:

$$\frac{1}{c}\frac{\partial}{\partial\rho}c = 0 \tag{34}$$

and

$$\frac{1}{c}\frac{\partial}{\partial a^i}c = \begin{cases} -\mu^i/\mu & i \in [coh,\ inc] \\ -\mu^i/\mu + 1/a^i & i = phot\ . \end{cases} \tag{35}$$

The relative double derivatives are then

$$\frac{1}{c}\frac{\partial}{\partial a^i}\frac{\partial}{\partial a^j}c = \begin{cases} 2\dfrac{\mu^i}{\mu}\dfrac{\mu^j}{\mu} & i \text{ and } j \in [coh, inc] \\ 2\dfrac{\mu^i}{\mu}\dfrac{\mu^j}{\mu} - \dfrac{\mu^j}{a^i\mu} & i = phot,\ j \in [coh, inc] \\ 2\dfrac{\mu^i}{\mu}\dfrac{\mu^j}{\mu} - 2\dfrac{\mu^i}{a^i\mu} & i = j = phot\ . \end{cases} \tag{36}$$

IV.B.2. Total Flux

For flux computed by the path-length estimator, the contribution to the tally is $c = s/V$, where s is the path length through the region. This is not dependent on any of the parameters used in this study, so the derivatives and double derivatives are all zero.

IV.B.3. Exposure

For exposure in a region, the path-length estimator is also used. The contribution to the tally is the product of the path length s, the current energy E, and the mass attenuation of air (at STP) at that energy $(\mu_{en}(E)/\rho)_{air}$, giving $c = (e/w)(sE/V)(\mu_{en}(E)/\rho)_{air}$, where e is the electron charge and w is the amount of energy needed to ionize air. This is not dependent on any of the parameters used in this study, so like with the total flux contribution, the derivatives and double derivatives are all zero.

IV.B.4. Dose

Because of the low X-ray energies, secondary electrons are not tracked. For the calculation of dose in a region (energy deposited divided by the mass of the region) in an analog game, the contribution to the response tally is simply $c = E_d/\rho V$, where E_d is the energy deposited (current E for photoelectric or E_e for incoherent scatter) and V is the volume of the region. The derivatives of the contribution with respect to parameters of the same region are

$$\frac{1}{c}\frac{\partial}{\partial \rho}c = -1/\rho \tag{37}$$

and

$$\frac{1}{c}\frac{\partial}{\partial a^i}c = 0\ . \tag{38}$$

The relative second derivative with respect to the density of the region is

$$\frac{1}{c}\frac{\partial^2}{\partial \rho^2}c = 2/\rho^2\ . \tag{39}$$

If implicit capture is being used, at each interaction, the contribution of

$$c = \frac{E}{\rho V}\frac{a^{phot}\mu^{phot}}{\mu} \tag{40}$$

is scored to the dose tally. The derivatives of this contribution with respect to parameters of the same region are

$$\frac{1}{c}\frac{\partial}{\partial \rho}c = -1/\rho \tag{41}$$

and

$$\frac{1}{c}\frac{\partial}{\partial a^i}c = \begin{cases} -\mu^i/\mu & i \in [coh, inc] \\ -\mu^i/\mu + 1/a^i & i = phot\ . \end{cases} \tag{42}$$

The relative double derivatives are

$$\frac{1}{c}\frac{\partial^2}{\partial \rho^2}c = 2/\rho^2\ , \tag{43}$$

$$\frac{1}{c}\frac{\partial}{\partial a^i}\frac{\partial}{\partial a^j}c = \begin{cases} 2\dfrac{\mu^i}{\mu}\dfrac{\mu^j}{\mu} & i \text{ and } j \in [coh, inc] \\ 2\dfrac{\mu^i}{\mu}\dfrac{\mu^j}{\mu} - \dfrac{\mu^j}{a^i\mu} & i = phot,\ j \in [coh, inc] \\ 2\dfrac{\mu^i}{\mu}\dfrac{\mu^i}{\mu} - 2\dfrac{\mu^i}{a^i\mu} & i = j = phot\ , \end{cases} \tag{44}$$

and

$$\frac{1}{c}\frac{\partial}{\partial a^i}\frac{\partial}{\partial \rho}c = \begin{cases} -\dfrac{\mu^i}{\rho\mu} & i \in [coh, inc] \\ -\dfrac{\mu^i}{\rho\mu} + \dfrac{1}{a^i\rho} & i = phot \ . \end{cases} \tag{45}$$

IV.B.5. Point Detector

For creating the scattered image, at each interaction point, the code computes the probability of both a coherent and incoherent scatter to each pixel in the image. This is very similar to the point-detector scheme used in many codes. The contribution to a pixel of area A and normal vector $\hat{n}$, and located in direction $\vec{\Omega}'$ from the interaction site and interaction type j (coherent or incoherent scatter) occurring in region M is

$$c_j = \frac{a_M^j \mu_M^j}{\mu_M} P^j(\mathbf{\Omega}, E \to \mathbf{\Omega}', E') \exp\left(-\sum \rho_m \mu_m' s_m\right) \frac{A\mathbf{\Omega}' \cdot \hat{n}}{\left(\sum s_m\right)^2} \ , \tag{46}$$

where s_m is the distance traveled through the various regions between the interaction site and the image pixel. After the scatter, the energy may change, and the new mass attenuation coefficients μ_m' (and each of their component cross sections) are evaluated at the new energy.

The derivatives of the contribution are

$$\frac{1}{c_k}\frac{\partial}{\partial \rho_m} c_k = -\mu_m' s_m \tag{47}$$

and

$$\frac{1}{c_k}\frac{\partial}{\partial a_m^j} c_k = \begin{cases} -\rho_m(\mu_m^j)' s_m & m \neq M \\ -\rho_m(\mu_m^j)' s_m - \mu_m^j/\mu_m & m = M, \ j \neq k \\ -\rho_m(\mu_m^j)' s_m - \mu_m^j/\mu_m + 1/a_m^j & m = M, \ j = k \ . \end{cases} \tag{48}$$

The second derivatives are

$$\frac{1}{c_k}\frac{\partial^2}{\partial \rho_m^2} c_k = (\mu_m s_m)^2 \tag{49}$$

and

$$\frac{1}{c_k}\frac{\partial^2}{\partial (a_m^j)^2} c_k = \begin{cases} (\rho_m(\mu_m^j)' s_m)^2 & m \neq M \\ (\rho_m(\mu_m^j)' s_m)^2 + 2\left(\dfrac{\mu_m^j}{\mu_m}\right)^2 + 2\dfrac{\mu_m^j}{\mu_m}\rho_m(\mu_m^j)' s_m & m = M, \ j \neq k \\ (\rho_m(\mu_m^j)' s_m)^2 + 2\left(\dfrac{\mu_m^j}{\mu_m}\right)^2 + 2\dfrac{\mu_m^j}{\mu_m}\rho_m(\mu_m^j)' s_m & \\ \qquad - 2\dfrac{1}{a_m^j}\left(\rho_m(\mu_m^j)' s_m + \dfrac{\mu_m^j}{\mu_m}\right) & m = M, \ j = k \ . \end{cases} \tag{50}$$

The point-detector algorithm was only used in calculating the scattered image. Because of space limitations, only the derivative and second derivative of the image with respect to one parameter is found by MCMIS-DS. With this limitation, cross derivatives such as $(\partial/\partial a_m^j)(\partial/\partial \rho_m)c_k$ are not needed.

IV.C. Implementation

Implementing the differential-sampling scheme for the responses (four tallies and the images) of the MCMIS code is fairly simple. For every response r, a subtally $q(r)$ is kept. At the end of each history, the subtallies are added to the main tallies, and the squares of the subtallies are added to the main variance tallies. For each combination of response r and parameter a, a derivative subtally $q(r,a)$ is kept. Similarly, for every combination of response, parameter a and parameter b, a second derivative subtally $q(r,a,b)$ is kept. At the end of each history, these subtallies are added to the main derivative tallies, and their squares are added to the derivative variance tallies.

Independent of the responses, other accumulators are kept. For every parameter a, the accumulator t_a is kept as an element of an array $t(a)$ for the current sum of the relative derivatives of the kernels. For every pair of parameters, the two types of second derivative accumulators $t_{1,a,b}$ and $t_{2,a,b}$ are kept in two other arrays, $t_1(a,b)$ and $t_2(a,b)$. These accumulators follow the photon path, similar to the weight of the photon. (Here we have dropped the i superscript denoting the i'th history. It is clear that the same accumulators can be cleared and reused with each history. The j superscript has also been dropped since these accumulate over each segment for the history.)

During a history, the accumulators t_a, $t_{1,a,b}$, and $t_{2,a,b}$ are updated at every transport step and collision for every parameter a and b. The subtally for a particular response derivative is updated only when the subtally for that response is updated. In general, whenever a subtally for a response is about to be updated, the following also occur:

1. Calculate the segment contribution to the tally (tally number Z) as c_{ij} and set the tally score as the photon weight multiplied by the segment contribution $score = wc_{ij}$.

2. Calculate all relative derivatives and double derivatives of c_{ij}.

3. Update the response subtally $q(Z) = q(Z) + score$.

4. Update every derivative subtally with respect to every parameter a

$$q(Z,a) = q(Z,a) + score \times \left(\frac{1}{c_{ij}} \frac{\partial}{\partial a} c_{ij} + t(a) \right) .$$

5. Update every second derivative subtally

$$\begin{aligned} q(Z,a,b) = q(Z,a,b) + score \\ \times \Bigg(t_1(a,b) - t_2(a,b) + t(a)t(b) \\ + \frac{1}{c_{ij}} \frac{\partial^2}{\partial a \partial b} c_{ij} + t(b) \frac{1}{c_{ij}} \frac{\partial}{\partial a} c_{ij} \\ + t(a) \frac{1}{c_{ij}} \frac{\partial}{\partial b} c_{ij} \Bigg) . \end{aligned}$$

Note that the current values up to this segment of w, $t(a)$, $t(b)$, $t_1(a,b)$, and $t_2(a,b)$ are used here.

At the end of a history, the response subtallies are added to the main tallies, and the squares of the subtallies are added to the variance tallies. The same procedure is used for the first derivative subtallies and the double-derivative subtallies.

After all N histories of the simulation are complete, the final calculations can be performed. First, the final responses are found by dividing the tally by the number of histories, and the associated standard deviation is found. Then, the derivatives of the responses are found by dividing the derivative tallies by the number of histories, and then their standard deviations are calculated.

IV.D. Results

A simple test can be used to demonstrate that this differential-sampling scheme is calculating the right values of the derivatives. Simulations of a 1.5-cm-thick piece of Lucite in a 20-keV synchrotron imaging beam were made at a set of values of the Lucite density or the values of the coefficients in the cross section $\mu = a^{phot}\mu^{phot} + a^{coh}\mu^{coh} + a^{inc}\mu^{inc}$. Within each set, the other parameters were kept constant at their nominal values. Each simulation calculated the four responses (E_d, ϕ, X, and D) in the Lucite slab—the derivatives with respect to each parameter and the second derivatives with respect to each parameter.

By comparing the derivatives calculated by differential sampling to the derivatives estimated from the responses calculated by the separate runs of a set, the validity of the differential sampling can be shown. This is done in Fig. 3 for the dose with respect to the Lucite density and in Fig. 4 for the energy deposited with respect to the coefficient for photoelectric absorption. Figures 3a and 4a show the response at the various values of the parameter. Figures 3b and 4b show the derivative of the response with respect to the parameter calculated by differential sampling (the points) and the estimate of the derivative (line) by taking the derivative of a polynomial fitted to the Monte Carlo responses. Figures 3c and 4c show the second derivative of the response with respect to the parameter calculated by differential sampling (the points) and the estimate of the derivative (line) by taking the derivative of a polynomial fitted to the Monte Carlo first derivatives.

The variance of the derivatives calculated by the differential-sampling method outlined in this paper were also checked to see if they correctly predicted the stochastic variance. The variance found in one hundred separate Monte Carlo runs using different random seeds did indeed match the average of the variances predicted by differential sampling for those runs.

V. MCMIS-DS WITH A BREASTLIKE PHANTOM

To show how differential sampling can be applied to mammography problems, a series of simulations and

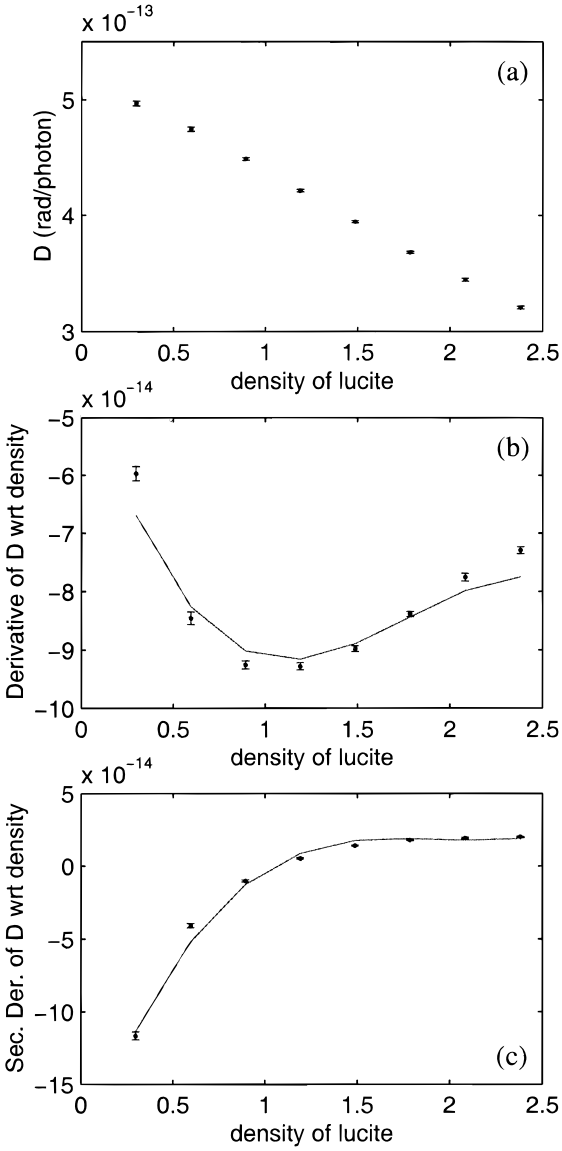

Fig. 3. (a) Dose (rad/photon) in a slab of Lucite for different values of the density, (b) $\partial D/\partial \rho$, and (c) $\partial^2 D/\partial \rho^2$. The points with error bars are from independent Monte Carlo calculations. The lines in (b) and (c) are the derivatives of the curve fit of the Monte Carlo data points from (a) and (b), respectively.

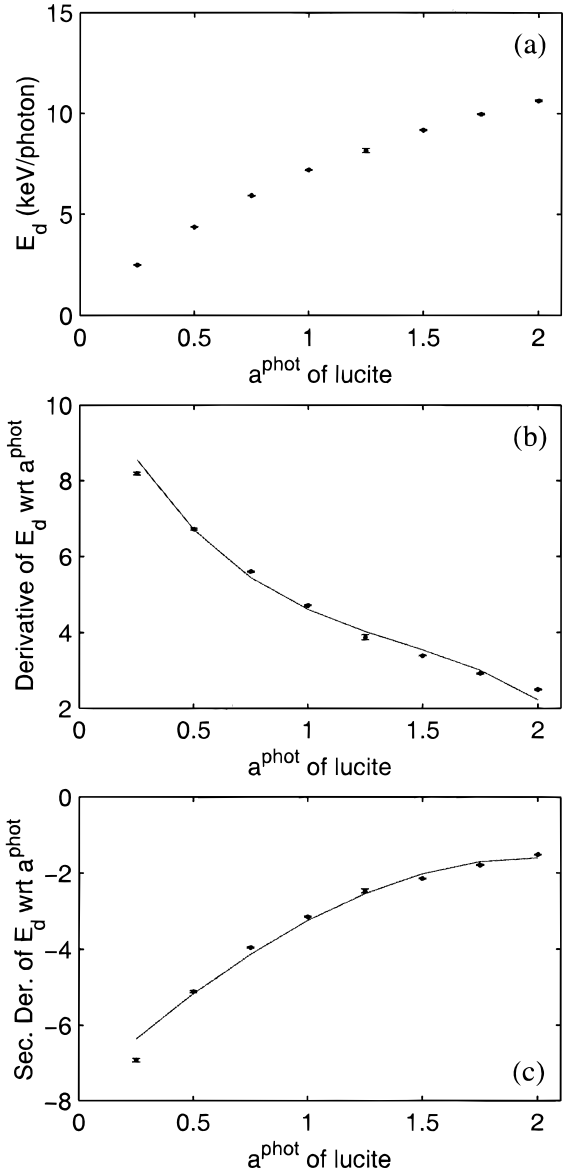

Fig. 4. (a) Energy deposited (keV/photon) in a slab of Lucite for different values of the photoelectric cross-section coefficient, (b) $\partial E_d/\partial a^{phot}$, and (c) $\partial^2 E_d/\partial (a^{phot})^2$. The points with error bars are from independent Monte Carlo calculations. The lines in (b) and (c) are the derivatives of the curve fit of the Monte Carlo data points from graphs (a) and (b), respectively.

calculations were carried out for a 4-cm-thick compressed breast in the Fischer Senoscan imaging system. The two questions that will be answered by the code are as follows. First, what is the sensitivity of the dose to the breast tissue with respect to the parameters of the breast tissue and the tumor tissue? Second, what density increase must a tumor have over that of ordinary breast tissue to be visible in the image? Both of these questions are important in medical physics, and they can be answered by using MCMIS-DS.

The reference model for the simulations included a compressed breast, consisting of ICRU 50/50 water/lipid whole breast material,[16] with a spherical tumor of the same material in the center. The breast is covered with a 0.4-cm-thick skin layer that is also made of this material. A cross section of this geometry is shown in Fig. 5, which also shows very thick skin on the sides of the breast. This was done so that doses reported for the simulations include only the breast material in the center portion of

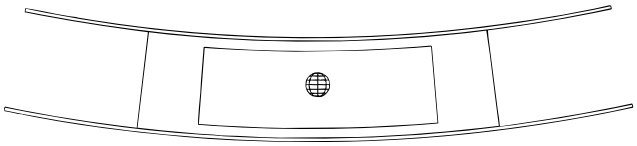

Fig. 5. Geometry of the compressed breast simulation using the Fischer Senoscan. The breast support and compression paddle hold the breast tissue to a 4-cm thickness. Only the center portion is used for the dose calculations; the rest is considered skin.

the breast. Skin dose tolerance limits are much higher than for the breast tissue.

In addition to the geometry shown in Fig. 5, the Fischer scanning-slot detector system was used in the simulation. The measured coherent scattering form factor of human breast tissue[8] was used for the breast, skin, and tumor regions. For the images, a pixel size of 100 μm was used for the fine-mesh images (unscattered, first derivative, and second derivative), and a pixel size of 0.5 cm was used for the coarse-mesh images (scatter and its derivatives).

To simulate a 25-kVp mammogram on the Senoscan, 20 monoenergetic simulations were made from 6 to 25 keV, at every 1 keV. The X-ray spectrum for a tungsten anode tube was taken from Boone, Fewell, and Jennings[17] and used as a weighting function to add together the monoenergetic images, the dose information, and the sensitivity information.

For each monoenergetic code run, an average of 6.5 min on a Sun Ultra 60 was required to create the three fine-mesh unscattered images. For the coarse-mesh scattered images, an average of 2.25 h was required. The scattered-to-primary (S/P) ratio for this simulation of a 4-cm compressed breast was 20% for most of the breast, with lower values toward the edges of the irradiation field. With this large an S/P ratio, the times for the scattered image calculations were selected to reduce the uncertainty in the polyenergetic scattered image to <2% over most of the image. In total, for one polyenergetic Senoscan simulation, 48 h of computer time on a Sun Ultra 60 were required.

V.A. Sensitivity of Breast Region Dose

To answer the first question about the sensitivity of the dose in the breast tissue, each monoenergetic run of MCMIS-DS found the derivatives of all of the tallies for the breast region with respect to all of the parameters of the breast region and the tumor region. The results of these runs were then added together with the same source spectrum weighting function to find the sensitivities for the polyenergetic spectrum. In addition to the tallies for the breast region, 32 first derivatives and 256 double derivatives were found. A few of the quantities calculated by MCMIS-DS for the combined 25-kVp spectrum are listed in Table 1.

TABLE I

A Few of the Tallies and Derivatives for the Breast Region at 25-kVp Calculated by MCMIS-DS

Quantity (per source photon)	Value
Energy deposited, E (keV)	3.643 ± 0.15%
Total flux, ϕ (cm^{-2})	0.001303 ± 0.16%
Dose, D (rad)	1.975E−13[a] ± 0.15%
$\partial D/\partial\rho$ (cm^3/g)	−1.372E−13 ± 0.24%
$\partial D/\partial a_{phot}$ (rad)	6.401E−14 ± 0.3%
$\partial D/\partial a_{coh}$ (rad)	2.288E−17 ± 270%
$\partial D/\partial a_{inc}$ (rad)	1.776E−15 ± 4.2%
$\partial^2 D/\partial\rho^2$ (cm^6/g^2)	−8.584E−14 ± 0.18%
$\partial^2 D/\partial a_{phot}^2$ (rad)	−7.188E−14 ± 0.18%
$\partial^2 D/\partial a_{coh}^2$ (rad)	3.93E−15 ± 0.54%
$\partial^2 D/\partial a_{inc}^2$ (rad)	6.76E−15 ± 0.6%

[a]Read as 1.975×10^{-13}.

From these values, the sensitivities of the breast dose to the different parameters were found. These sensitivities are displayed in Table II, and from them, it is clear that the dose in the breast region is much more sensitive to the parameters of itself than to the parameters of the tumor region. Further analysis shows that the dose is more sensitive to the breast tissue density (or its total cross section) and the photoelectric cross section than to either of the scattering cross sections.

The foregoing information can also be used in propagating errors. The 0.15% relative uncertainty reported in Table I for the dose to the central portion of the breast is the stochastic error only. Using the value for $(\rho/D)(\partial D/\partial\rho_{breast})$, one could determine that a 1% uncertainty in the breast tissue density gives an ~0.64% uncertainty in the dose value. A similar 1% uncertainty in the tumor density gives only a 0.00067% uncertainty in the dose, which makes sense considering how little the density of a small tumor should affect the absorbed dose in the breast. These uncertainties could then be combined with the stochastic uncertainty to give the total uncertainty in the dose value.

V.B. Tumor Density and Visibility

For the second question of what density difference a certain size tumor must have in order to be visible in the image, the code was instructed to find the derivatives of the images with respect to the density of the tumor region. These were calculated at the same time as the foregoing sensitivity figures.

The runs computed the images from a breast that contained a tumor of the same density, which is referred to

TABLE II

Sensitivities for the Breast Region Calculated from the Doses and Derivatives Found Using MCMIS-DS

Quantity	Parameters in the	
	m = breast	m = tumor
$\frac{\rho_m}{D}\frac{\partial D}{\partial \rho_m}$	−0.6390 ± 0.28%	−6.708E−4[a] ± 5.8%
$\frac{a_m^{phot}}{D}\frac{\partial D}{\partial a_m^{phot}}$	0.3241 ± 0.33%	−8.066E−4 ± 3.4%
$\frac{a_m^{coh}}{D}\frac{\partial D}{\partial a_m^{coh}}$	1.158E−4 ± 270%	2.508E−05 ± 50%
$\frac{a_m^{inc}}{D}\frac{\partial D}{\partial a_m^{inc}}$	8.993E−3 ± 4.2%	8.15E−05 ± 23%

[a]Read as -6.708×10^{-4}.

here as the reference case. Obviously, a tumor of the same composition and density as the surrounding tissue would not be visible in the images. But, MCMIS-DS also computed the first and second derivatives of the image with respect to tumor density. For a 1-cm tumor, both sets of Monte Carlo unscattered and scattered images are shown in Fig. 6. From these images, an image can be created from a Taylor series expansion for a tumor of any density close to the reference case. Of course, real clinical images would not have such a smooth background as the tissue structure of glands, and fat would be visible and would somewhat hide the tumor. Ignoring this fact for the moment, this example is still useful in showing an application of differential sampling and in providing useful information for system designers and medical physicists.

For a 1-cm-diam tumor, the images shown in Fig. 6 were combined in a truncated Taylor series for six different tumor densities:

$$I(\rho + \delta\rho) = I(\rho_0) + \left(\frac{\partial I}{\partial \rho}\right)\delta\rho + \frac{1}{2}\left(\frac{\partial^2 I}{\partial \rho^2}\right)(\delta\rho)^2 \ , \tag{51}$$

$$\rho_0 = 0.92 \text{ g/cm}^3 \ , \tag{52}$$

and

$$\delta\rho \in \rho_0 \times [0.01, 0.015, 0.02, 0.025, 0.03, 0.05] \ . \tag{53}$$

These images were then processed by adding 0.5% relative noise (typical in Senoscan images) and applying the MTF. The final six images are shown in Fig. 7. From this series of images, one can judge what level of density difference is required before the tumor is visible. Clearly, at a 2.0% density increase over that of the surrounding tissue, the tumor is visible, and different observers may argue about visibility at the lower-density increases.

Series of images for smaller tumor sizes, 0.5 cm and 0.25 cm diameter, are shown in Figs. 8 and 9. The 0.5-cm tumor is not visible until at least a 2.5% increase in tumor density over tissue density (again, other observers may argue). The smallest tumor (0.25 cm) is not visible until a density increase of 5% over that of normal tissue. This kind of information is very useful in comparing different mammography systems or in optimizing the spectrum or other system parameters for a single system.

The real benefit of the differential sampling and Taylor series approach is the ability to return to the problem later and add another value of $\delta\rho$ without running any more Monte Carlo calculations. Once the reference case image and its derivatives have been calculated, any number of images can be made with different tumor densities. This is one big advantage of differential sampling over correlated sampling. In fact, since the polyenergetic spectrum was made of the weighted sum of monoenergetic spectra, the spectrum could be changed, and the study could be repeated without running any more Monte Carlos.

Similar perturbation calculations can be made for the tallies in the breast region with the output from MCMIS-DS that was shown in Tables I and II. For any change in the parameters of either the breast tissue or the tumor (or both simultaneously), one could calculate the new quantities.

VI. SUMMARY

We have formulated and implemented differential sampling in a Monte Carlo code specifically written to

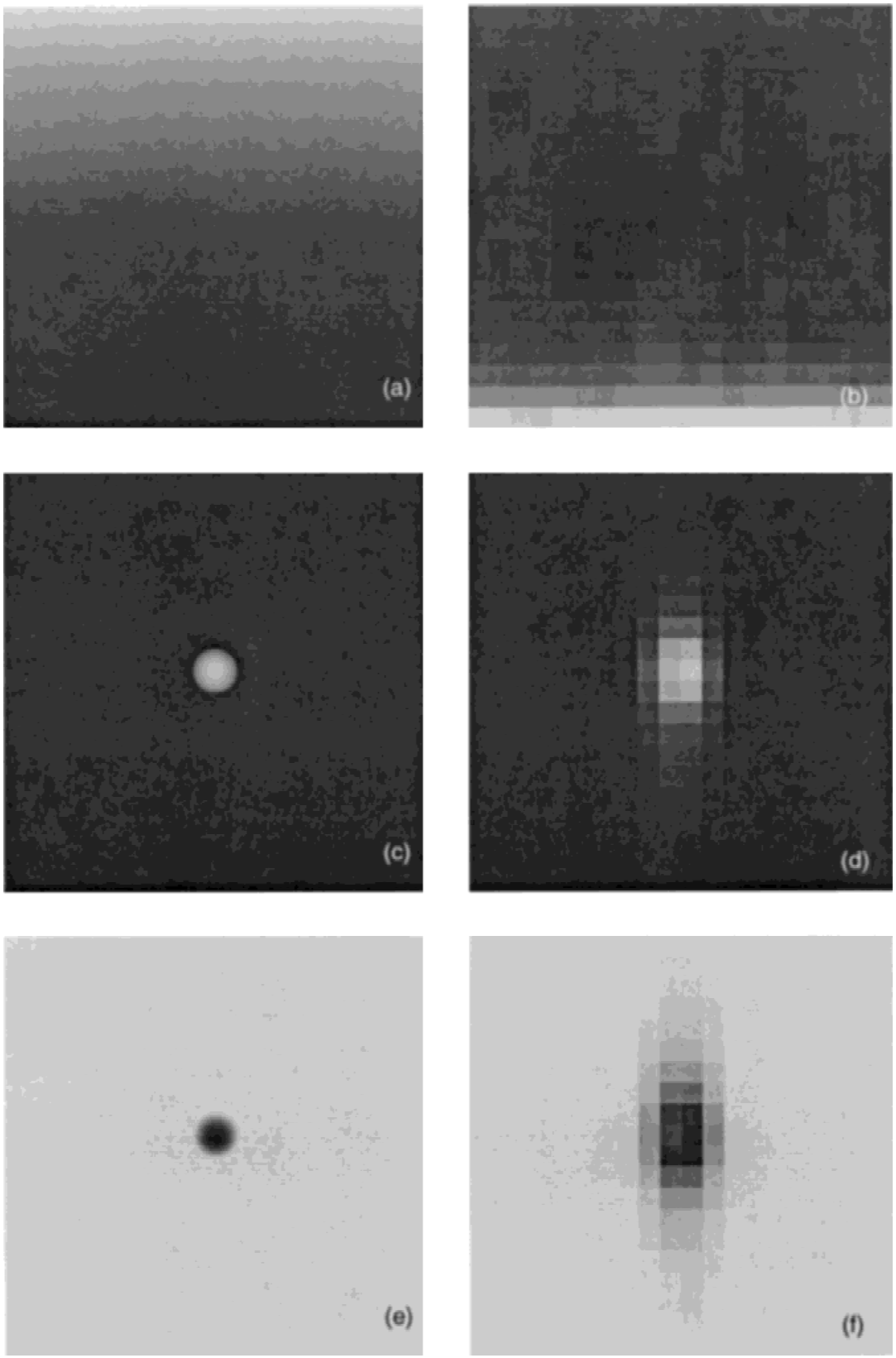

Fig. 6. Monte Carlo images created by MCMIS-DS for the breast/tumor problem: (a) The unscattered image, (b) the scattered image (c) and (d) the first derivative with respect to tumor density (unscattered and scattered). The second derivatives are also shown in panels (e) and (f).

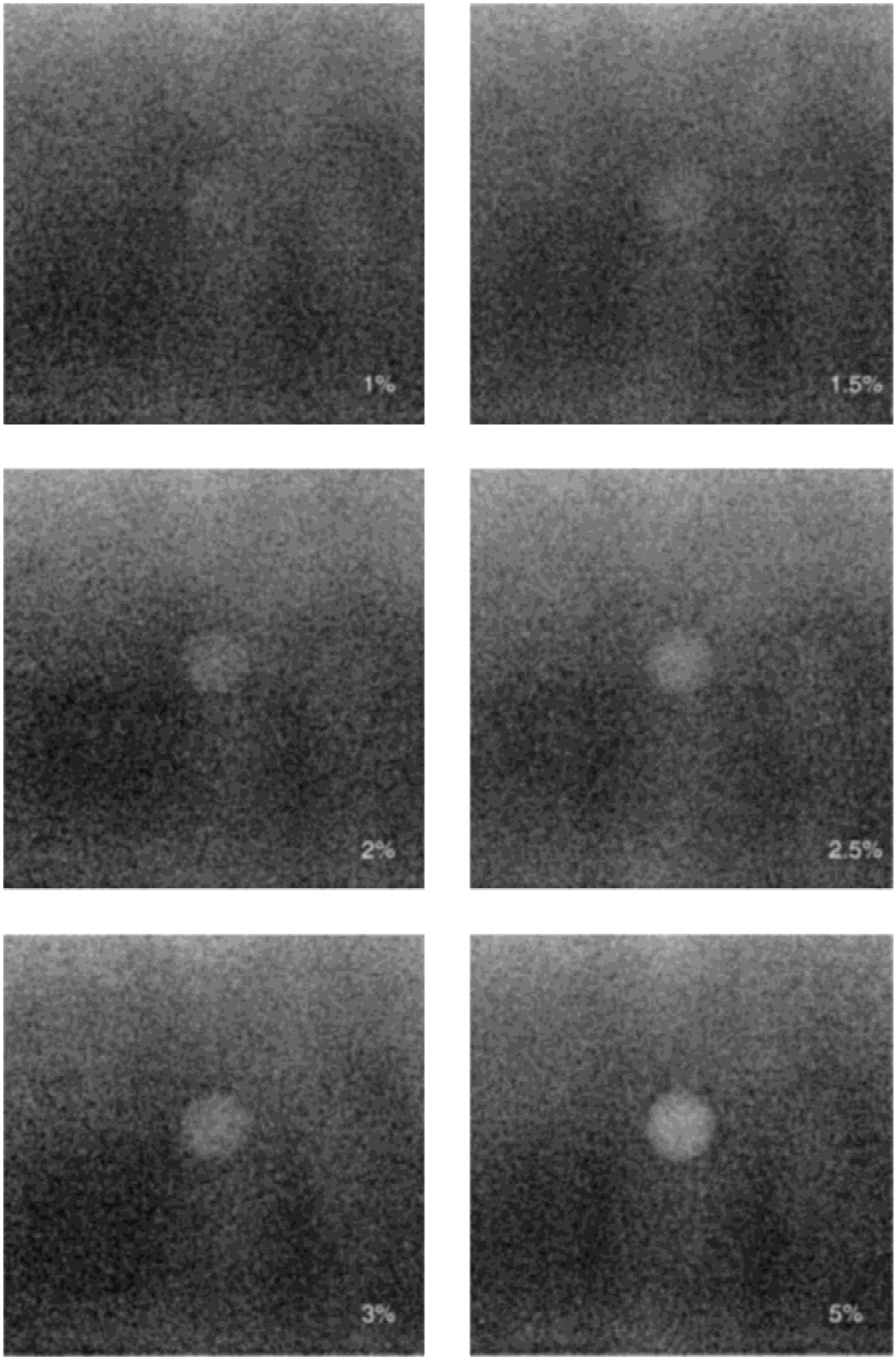

Fig. 7. Six images created by a truncated Taylor series for a 1-cm tumor. Each panel is labeled with the percentage increase in tumor density over that of the breast tissue. Noise and the system MTF have been added to these images, simulating what the Fischer Senoscan would see for a 4-cm compressed breast.

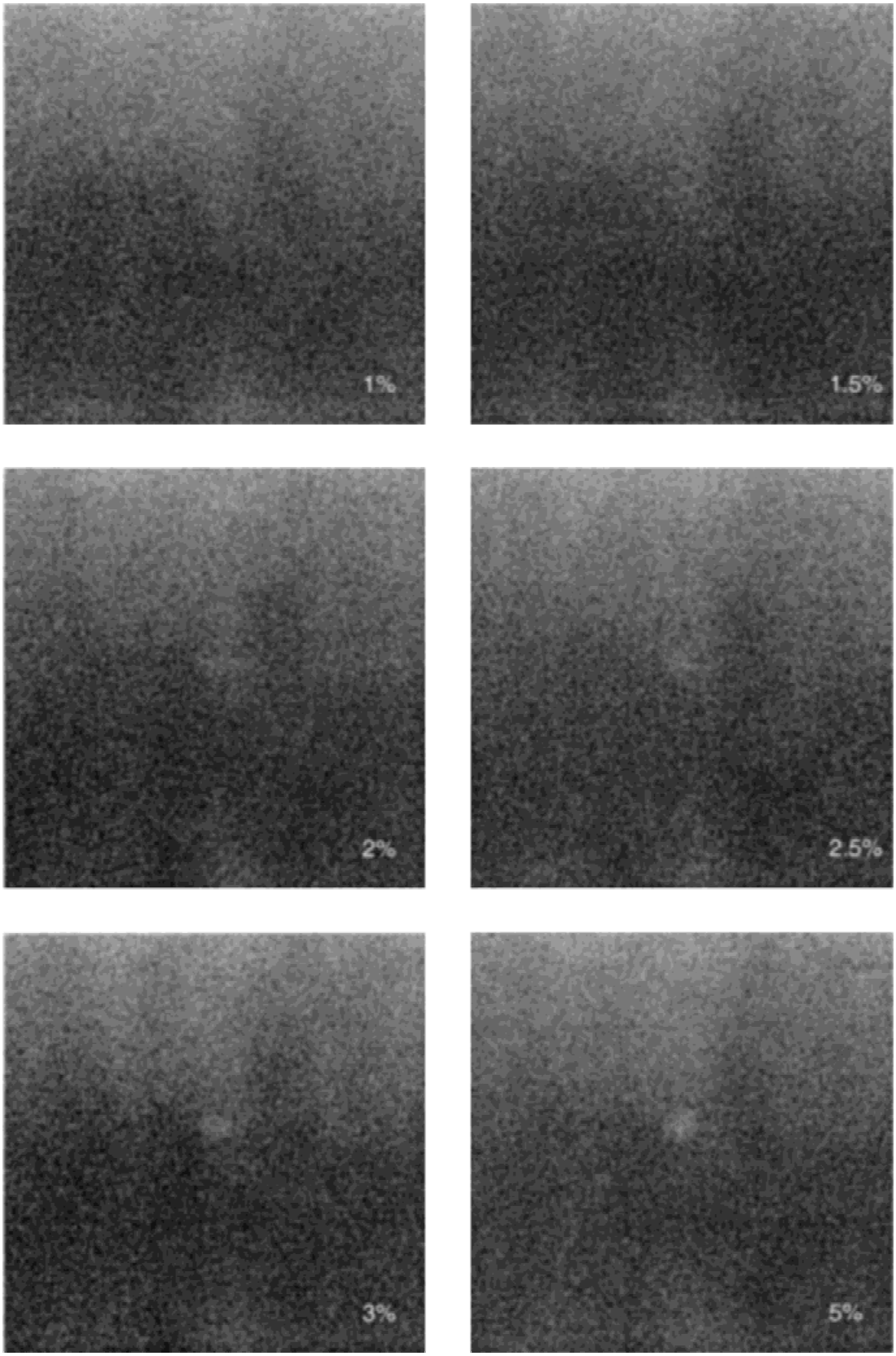

Fig. 8. Six images created by a truncated Taylor series for a 0.5-cm tumor. Each panel is labeled with the percentage increase in tumor density over that of the breast tissue. Noise and the system MTF have been added to these images.

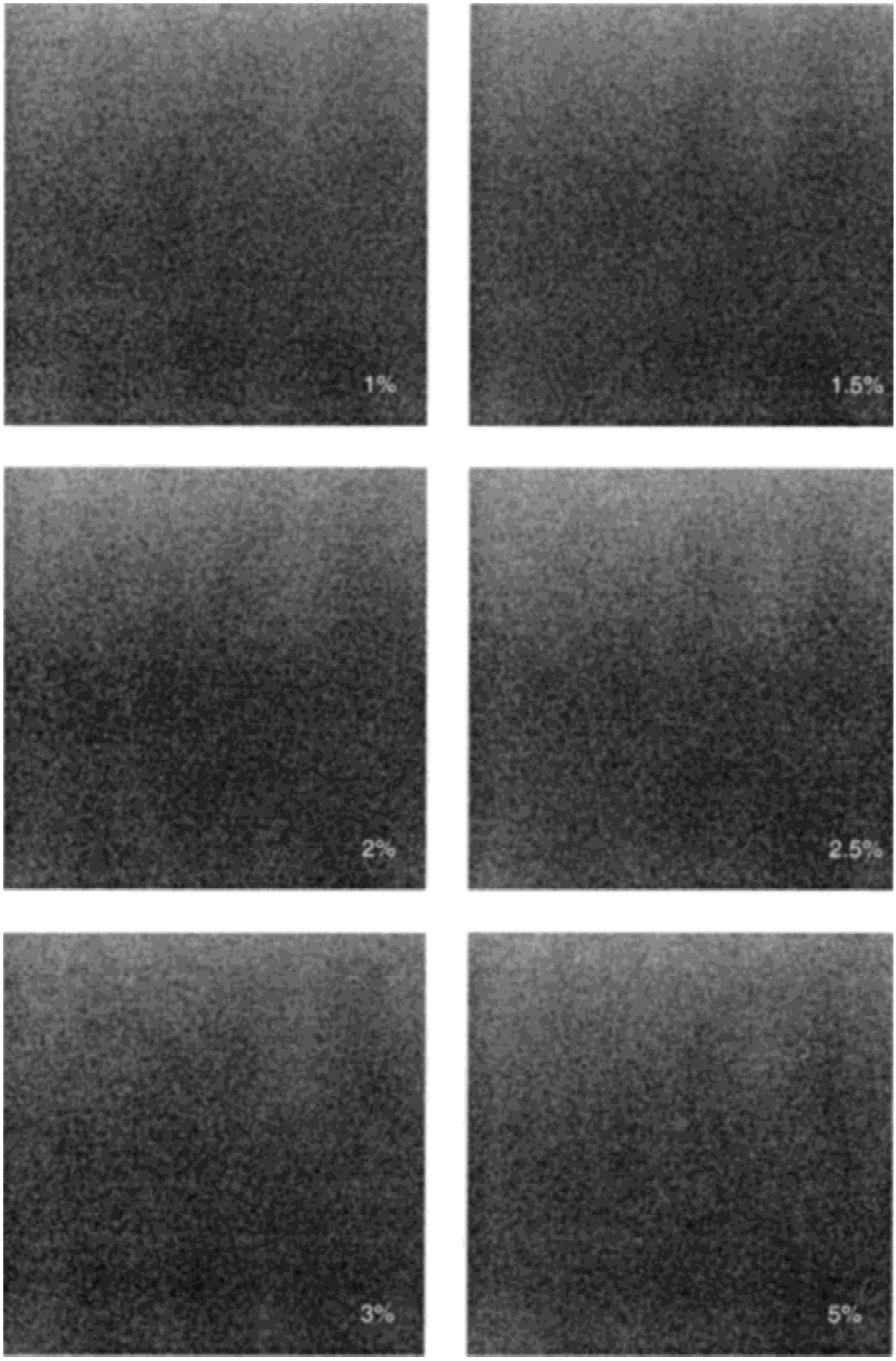

Fig. 9. Six images created by a truncated Taylor series for a 0.25-cm tumor. Each panel is labeled with the percentage increase in tumor density over that of the breast tissue. Noise and the system MTF have been added to these images.

simulate two new and advanced digital mammography systems. The code uses experimentally measured coherent scattering angular distributions of X rays in mammographically relevant materials[8] and simulates images on 2048×2048 pixels and also calculates the exposure and the absorbed dose to the sample.[5] A variety of variance-reduction schemes were used to make the image simulation possible on standard computing platforms. The simulated results showed good fidelity in their comparison to experimental benchmarks on both systems.

Since it is a perturbation technique, differential sampling can reveal a great deal of information without adding much computational cost. Its application to Monte Carlo problems with variance-reduction methods is no more difficult than to analog Monte Carlo simulations. Also, responses to perturbations of several system parameters can be calculated simultaneously. Since the derivatives of responses and their variances are tallied, the responses for other variations in the parameter values can be computed at a later time without having to re-run the code. This is a considerable advantage over the method of correlated sampling. The methods presented in this paper make the implementation of differential sampling much easier for a Monte Carlo code developer when compared to the descriptions presented in the past in literature.

Our code, MCMIS-DS, gives the user considerably greater flexibility in exploring mammography images that can be expected for parameter changes than any standard code could give. Two examples are shown as demonstrations of the implementation of differential sampling. In the first example, we have shown how to formulate differential sampling for a dose-related problem involving four dose-related tallies for perturbations in sample density and cross sections. The main thrust here has been to demonstrate that the response derivatives calculated by differential sampling and their variance agree exactly with the numerical derivatives of the response and their stochastic variance. In the second example problem, we investigated two medically relevant questions, namely, the sensitivity of the X-ray dose to the breast as a function of tumor and normal tissue parameters and the discernibility of tumors of different sizes in an image of the breast as a function of tumor density in the case of one of the two mammography modalities (Fischer Senoscan).

It should be stressed that the MCMIS-DS code itself is not as important a part of this paper as the ideas used in its development. The description of differential sampling and its application to the mammography image simulation package are expected to provide others with the ability to adapt and implement differential sampling for their own applications.

Concerning mammography studies, it has been shown that a tool with the capabilities of MCMIS-DS can provide useful information. In sensitivity analysis and perturbation studies, these tools are very useful in comparing imaging systems and in designing and optimizing single systems. In the future, the concepts of the MCMIS and MCMIS-DS package will be refined and built into a tool for the mammographic imaging community.

Basic research into differential sampling also needs to continue. Two parameters were not explored in this project, and they are very important to medical imaging: the source energy of the photons E_0 and the physical dimensions s of regions. Similar types of parameters as these two are also important in many other areas, and it would be of great benefit if differential sampling could be used for perturbations of these parameters. More research is required to do one of the following: either show how differential sampling can calculate $\partial/\partial s$ and $\partial/\partial E_0$ or show conclusively that these derivatives cannot be calculated.

ACKNOWLEDGMENTS

Research was carried out in part at the National Synchrotron Light Source, Brookhaven National Laboratory, which is supported by the U.S. Department of Energy (DOE), Division of Materials Sciences and Division of Chemical Sciences. Many thanks to W. C. Thomlinson and Z. Zhong for allowing this work to be done on beamline X15A.

R. E. Johnston of the University of North Carolina, Chapel Hill, provided assistance in both the synchrotron imaging and Senoscan imaging aspects of this study. We thank him for all of his valuable help.

The first author (D.E.P.), at the time a doctoral student, was supported by R. E. Johnston through his U.S. Army Medical Research and Material Command Breast Cancer Research Grant. He was also supported by a Nuclear Engineering Education Research Grant from the DOE Idaho Operations Office.

Thanks also to the referees who helped make this a better paper.

REFERENCES

1. R. E. JOHNSTON, D. WASHBURN, E. PISANO, C. BURNS, W. THOMLINSON, L. D. CHAPMAN, F. ARFELLI, N. GMÜR, Z. ZHONG, and D. SAYERS, "Mammographic Phantom Studies with Synchrotron Radiation," *Radiology*, **200**, 659 (1996).

2. F. ARFELLI, G. BARBIELLINI, V. BONVICINI, A. BRAVIN, G. CANTATORE, E. CASTELLI, L. DALLA PALMA, M. DI MICHIEL, R. LONGO, A. OLIVO, S. PANI, D. PONTONI, P. POROPAT, M. PREST, R. ROSEI, M. SESSA, G. TROMBA, and A. VACCHI, "Digital Mammography at the Trieste Synchrotron Light Source," *IEEE Trans. Nucl. Sci.*, **43**, 2061 (1996).

3. E. BURATTINI, E. COSSU, C. DI MAGGIO, M. GAMBACCINI, P. L. INDOVINA, M. MARZIANI, M. POECK, S. SIMEONI, and G. SIMONETTI, "Mammography with Synchrotron Radiation," *Radiology*, **195**, 239 (1995).

4. L. D. CHAPMAN, W. THOMLINSON, R. E. JOHNSTON, D. WASHBURN, E. PISANO, N. GMÜR, Z. ZHONG, R.

MENK, F. ARFELLI, and D. SAYERS, "Diffraction Enhanced X-Ray Imaging," *Phys. Med. Biol.*, **42**, 2015 (1997).

5. D. E. PEPLOW and K. VERGHESE, "Digital Mammography Image Simulation Using Monte Carlo," *Med. Phys.*, **27**, 568 (2000).

6. L. L. CARTER and E. D. CASHWELL, *Particle-Transport Simulation with the Monte Carlo Method*, Washington Technical Information Center, Office of Public Affairs, U.S. Energy Research and Development Administration (1975).

7. A. H. NARTEN, "X-Ray Diffraction Data on Liquid Water in the Temperature Range 4° to 200°C," ORNL-4578, Oak Ridge National Laboratory (1970).

8. D. E. PEPLOW and K. VERGHESE, "Measured Molecular Coherent Scattering Form Factors of Animal Tissues, Plastics and Human Breast Tissue," *Phys. Med. Biol.*, **43**, 2431 (1998).

9. H. RIEF, "Generalized Monte Carlo Perturbation Algorithms for Correlated Sampling and a Second-Order Taylor Series Approach," *Ann. Nucl. Energy*, **11**, 455 (1984).

10. H. RIEF, "Monte Carlo Uncertainty Analysis," *Uncertainty Analysis*, Y. RONEN, Ed., CRC Press, Boca Raton, Florida (1988).

11. H. RIEF, "A Synopsis of Monte Carlo Perturbation Algorithms," *J. Comput. Phys.*, **111**, 33 (1994).

12. H. RIEF, "Stochastic Perturbation Analysis Applied to Neutral Particle Transport," *Adv. Nucl. Sci. Technol.*, **23**, 69 (1996).

13. R. L. PEREL, J. J. WAGSCHAL, and Y. YEIVIN, "Monte Carlo Calculation of Point-Detector Sensitivities to Material Parameters," *Nucl. Sci. Eng.*, **124**, 197 (1996).

14. D. E. PEPLOW and K. VERGHESE, "Differential Sampling for the Monte Carlo Practitioner," *Prog. Nucl. Energy*, **36**, 39 (2000).

15. "MCNP™—A General Monte Carlo N-Particle Transport Code," LA-12625-M, J. BRIESMEISTER, Ed., Los Alamos National Laboratory (1997).

16. ICRU, "ICRU 46: Photon, Electron, Proton, and Neutron Interaction Data for Body Tissues," Rep. 46 (1992).

17. J. M. BOONE, T. R. FEWELL, and R. J. JENNINGS, "Molybdenum, Rhodium, and Tungsten Anode Spectral Models Using Interpolating Polynomials with Application to Mammography," *Med. Phys.*, **24**, 1863 (1997).